Delft University of Technology

Design and modeling of a Laue lens for radiation therapy with hard x-ray photons

Girou, David; Ford, Eric; Wade, Colin; Van Aarle, Casper; Uliyanov, Alexei; Hanlon, Lorraine; Tomsick, John A.; Zoglauer, Andreas; Collon, Maximilien J.; More Authors

Important note
To cite this publication, please use the final published version (if applicable).
Please check the document version above.

Design and modeling of a Laue lens for radiation therapy with hard x-ray photons

To cite this article: David Girou *et al* 2021 *Phys. Med. Biol.* **66** 245007

View the article online for updates and enhancements.

You may also like
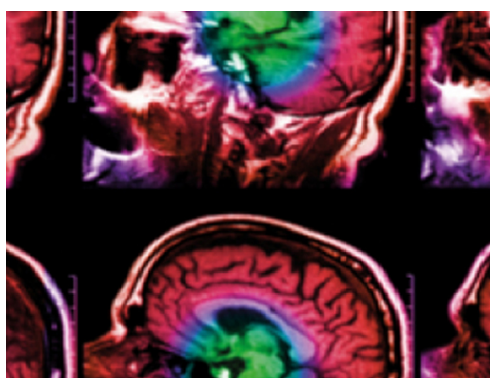
IPEM | IOP

Series in Physics and Engineering in Medicine and Biology

Your publishing choice in medical physics, biomedical engineering and related subjects.

Start exploring the collection–download the first chapter of every title for free.

Physics in Medicine & Biology

IPEM Institute of Physics and Engineering in Medicine

CrossMark

PAPER

Design and modeling of a Laue lens for radiation therapy with hard x-ray photons

David Girou[1,2] , Eric Ford[3], Colin Wade[1,4], Casper van Aarle[1,5], Alexei Uliyanov[4], Lorraine Hanlon[4], John A Tomsick[6], Andreas Zoglauer[6], Maximilien J Collon[1], Marco W Beijersbergen[1,2] and Nicolas M Barrière[1]

1   cosine measurement systems, Oosteinde 36, 2361 HE Warmond, The Netherlands
2   Huygens-Kamerlingh Onnes Laboratory, Leiden University, Postbus 9504, 2300 RA Leiden, The Netherlands
3   Department of Radiation Oncology, University of Washington, Seattle, WA 98195, United States of America
4   School of Physics and Centre for Space Research, University College Dublin, Belfield, Dublin 4, Ireland
5   Delft University of Technology, Faculty of Applied Sciences, Department of Radiation Science and Technology, Mekelweg 15, 2629 JB Delft, The Netherlands
6   Space Sciences Laboratory, University of California, Berkeley, 7 Gauss Way, Berkeley, CA 94720, United States of America

E-mail: d.girou@cosine.nl

Keywords: silicon Laure components, silicon pore optics, radiotherapy, hard x-rays, focused beam, focusing optics

Abstract

We have designed and modeled a novel optical system composed of a Laue lens coupled to an x-ray tube that produces a focused beam in an energy range near 100 keV ($\lambda = 12.4$ picometer). One application of this system is radiation therapy where it could enable treatment units that are considerably simpler and lower in cost than present technologies relying on linear accelerators. The Laue lens is made of Silicon Laue components which exploit the silicon pore optics technology. The lens concentrates photons to a small region thus allowing high dose rates at the focal area with very much lower dose rates at the skin and superficial regions. Monte Carlo simulations with Geant4 indicate a dose deposition rate of 0.2 Gy min^{-1} in a cylindrical volume of 0.7 mm diameter and 10 mm length, and a dose ratio of 72 at the surface (skin) compared to the focus placed 10 cm within a water phantom. Work is ongoing to newer generation crystal technologies to increase dose rate.

1. Introduction

Radiation therapy plays an essential role in the treatment of cancer, with more than 60% of patients receiving radiation therapy, mainly in the form of high-energy photons (2–20 MeV), in the course of their disease management (Atun *et al* 2015). Such high-energy photons present many challenges due to their penetrating power and the ionisation damage they cause to healthy, as well as diseased, tissue (Desouky *et al* 2015). The technology used in radiation therapy for cancer treatment can be used to exquisitely shape the radiation dose around a tumor inside a patient with a precision that is an order-of-magnitude better than twenty years ago. However, some tumors are still not curable. New approaches are being explored such as using radiation in combination with targeted agents such as immune-modulating drugs (Demaria *et al* 2005). While radiation therapy as a single-agent for cancer treatment may have reached the limits of its achievements, this modality is likely to be needed in the long term. As such, technology development efforts are well-justified (Allen *et al* 2017).

Radiotherapy uses ionizing radiation to damage the DNA of cancerous tissue causing cellular death and slowing cell growth. In external beam therapy, the radiation beam enters the patient on the surface, delivering a superficial dose D_S. Beneath the surface, the dose first rises rapidly with depth, reaching a maximum value at a depth d_{max}, and then decreases almost exponentially until it reaches an exit dose value at the patient's exit point (Khan 2003). The relatively low surface dose for high-energy photon beams (referred to as the skin-sparing effect) is of great importance in radiotherapy to treat deep-seated lesions without undue toxicity to the skin and superficial tissues. The tumor dose can be concentrated at deep depths in the patient while delivering a relatively low dose to the skin and other normal tissues at superficial depths which are not involved in the disease. The dose

region between the surface and the depth of dose maximum d_{max} is called the dose buildup region and represents the region in the patient in which the dose deposition rises with depth as a result of the range of secondary electrons released in tissue by photon interactions with the atoms of tissue. It is these secondary electrons released by photons that deposit energy in tissue (indirect ionization). The greater the photon energy, the more extensive the range of secondary electrons and, consequently, the larger the depth of dose maximum. These considerations have led to the almost exclusive use of MeV photon beams for radiotherapy.

However, the ability to deliver therapeutic treatments with low-energy radiation (<200 keV) would be attractive for several reasons. First, one could envision more cost-effective treatment units compared to the linear accelerator technologies currently required to create a high-fluence beam of tens of MeV energy. More reliable, cost-effective solutions are especially attractive as cancer therapy needs to expand in low- and middle-income countries which in some cases lack even a single treatment facility due to technology and cost barriers (Atun *et al* 2015).

Therapy beams at low energies may also be attractive in their ability to achieve increased sensitivity when used in combination with high-*Z* nanoparticles. Recent high-profile studies have shown that tumor cell survival is significantly reduced by combining x-ray irradiation with gold nanoparticles (Chithrani *et al* 2010). This reduction is due to dose enhancement in or near the cell, which results from photoelectric effects in the high-*Z* nanoparticle (Leung *et al* 2011). A large dose enhancement factor (66%) was observed for low energy x-rays (<200 keV). However, as described in the previous paragraph, it is not currently possible to deliver low-energy irradiation in the clinical setting without unacceptable toxicity to the skin and normal tissue. Medical physicists have therefore altered their approach (Berbeco *et al* 2012) and are now considering gold nanoparticles in combination with the high-energy beams which are routinely used in the clinic (mean energy ∼2 MeV). However, at these energies, the photoelectric interactions are orders of magnitude lower (Leung *et al* 2011) and therefore have a dose enhancement of only 10%–20% (Chithrani *et al* 2010). In summary, low-energy radiation (<200 keV) combined with high-*Z* nanoparticles would be extremely effective against tumor cells. However, it is not currently possible to deliver low-energy radiation to deep-seated tumors in a patient.

In this paper, we report a possible solution to create a converging beam, which spares the skin by spreading the dose over a large area. This is similar to the concept reported by Breitkreutz *et al* (2017) and references therein but instead of using a mechanical system with multiple sources and collimation, the present study uses an x-ray lens system. This is also different from polycapillary optics which work at lower energy and can thus not be used for deep-seated tumors (Abbas *et al* 2014). This is an update of work from our group presented by Wade *et al* (2018) where we investigated lens designs and assembly techniques. In the current paper, we first describe how silicon pore optics (SPO) technology can be used to create self-focusing Laue lens elements, the so-called Silicon Laue components (SiLCs). Then, we detail the method used to design such SiLCs, including the in-house Monte Carlo SiLC Simulation Code (SSC) we developed to simulate diffraction in SiLCs. Finally, we present the optimized lens design and show that this lens can provide an unprecedented ratio of dose at the surface (skin) compared to its focus, based on Geant4 (Agostinelli *et al* 2003, Allison *et al* 2006, 2016) simulations. Note that while obtaining different results (see section 4.3), the effort and methods detailed in this paper can be compared to the work of Paternò *et al* (2016) and Camattari (2017).

2. Silicon Laue components

A Laue lens is a concentrator that uses Bragg diffraction in the volume of symmetrically cut crystals (referred to as Laue geometry). Laue lenses are an emerging technology based on crystal diffraction that enables soft gamma-ray focusing. Laue lenses have the potential to overcome the limitations imposed by the depth dose distribution, thereby enabling the clinical use of low-energy photon beams for radiotherapy. In high-energy astrophysics, there have been significant efforts devoted to the development of a focusing gamma-ray technology (Lund 1992, 2005, Halloin *et al* 2003, Frontera and von Ballmoos 2010, Barrière *et al* 2014, Barrière *et al* 2017, Guidorzi *et al* 2021).

Diffraction lenses use the interference between the periodic nature of the electromagnetic radiation and a periodic structure such as the matter in a crystal. In order to be diffracted, an incoming gamma-ray must satisfy the Bragg condition:

$$2d_{hkl} \sin \theta = n \frac{hc}{E}, \tag{1}$$

where d_{hkl} (in Å) is the spacing of the lattice planes (hkl), n is the diffraction order, h is the Planck constant, c is the speed of light, and E is the energy of the gamma-ray photon.

In the transmission configuration, a Laue lens is made of many individual crystals that are arranged so that they will all diffract the incident radiation onto a common focal spot. For a given set of planes and order of

reflection, the Bragg condition is only met for a single energy. Mosaic crystals or curved crystals can be used to increase the bandpass. Mosaic crystals can be modeled as an assembly of perfect microscopic crystals (crystallites) whose lattice planes are slightly misaligned with each other around a mean direction, following a normal distribution (Halloin and Bastie 2005). Similarly, curved crystals have an angular dispersion of the lattice planes and a larger energy passband than perfect crystals. Though the downside is mosaic defocusing, i.e. the fact that the energy bandpass comes from a range of angular crystal plane orientation, but also results in a range of directions for the diffracted rays as a function of their wavelength. Curved crystals can be obtained in various ways, including the elastic bending of a perfect crystal (Ferrari *et al* 2013) (the technique commonly used in synchrotron radiation facilities), or the growing of a two-component crystal (Abrosimov *et al* 2005, Smither *et al* 2005) whose composition varies along the crystal growth axis, or the indentation of one face of a wafer (Bellucci *et al* 2011).

The diffracted flux from a continuum source increases with increasing mosaicity of mosaic crystals or the total bending angle of curved crystals (Halloin and Bastie 2005). For a Laue lens telescope, crystals with mosaicities or total bending angles ranging from a few tens of arcseconds to a few arcminutes are relevant. The bandwidth of a lens for an on-axis source is determined by the mosaicity or total bending angle of the individual crystals and by the accuracy of the alignment of the single crystals. The rectangular diffraction profiles of curved crystals produce more effective flux concentration than the Gaussian profiles of mosaic crystals (Barrière *et al* 2006). Curved crystals have higher peak diffraction efficiency (100% max.) than mosaic crystals (50% max.) due to the absence of extinction effects (Keitel *et al* 1999). However, Laue lenses constructed from either mosaic or curved crystals have several limitations. For instance, the smallest spot size that can be achieved is given by the size of the smallest crystal element in the lens. Also, the individual components of the lens are not focusing elements themselves. Furthermore, the assembly of the lens relies heavily on the accurate placing of many hundreds (or thousands) of crystal elements, which is challenging.

Laue lens technology has been slowly developing for several decades (Lindquist and Webber 1968, Frontera and von Ballmoos 2010, Barrière *et al* 2014, Wade *et al* 2018) and recently took a new turn with Silicon Laue Components (SiLCs) (Ackermann *et al* 2013) based on SPO technology. SPO are a new type of x-ray optics designed to enable future space-borne x-ray observatories such as Athena (Beijersbergen *et al* 2004). Since x-rays from celestial sources do not penetrate Earth's atmosphere, x-ray telescopes must be in space. SPO are being developed by the European Space Agency in collaboration with academic and industrial partners (Bavdaz *et al* 2019, Collon *et al* 2019). These high-performance, modular, lightweight yet stiff, high-resolution x-ray optics shall allow space telescopes to reach an unprecedentedly large effective area of a few square meters, operating in the 0.2–12 keV band with an angular resolution aiming at being better than 5 arcseconds. To this end, custom-made assembly tools and processes have been developed to build SPO using direct silicon bonding (Shimbo *et al* 1986, Maszara *et al* 1988). Because each SPO plate is a single side ribbed rectangular silicon substrate, stacking them results in a pore-like structure. X-ray photons enter these pores at low grazing angles, are reflected on the top side of each plate inside the pores, and exit the optics at the opposite end.

SPO technology can also be used to fabricate soft gamma-ray Laue lenses if Bragg diffraction through the bulk silicon is exploited, rather than grazing incidence reflection. A SiLC-based Laue lens can focus photons in the range ∼80 to ∼300 keV, and present several advantages over alternative Laue lens concepts. SiLCs are made of stacks of curved, polished, wedged silicon plates, and contrary to SPO, the individual plates are not ribbed. Each element is bent in two dimensions, with a meridional and a sagittal curvature. The direction of sagittal curvature is perpendicular to the optical axis, ensuring the normal vector to the plate's surface always points at the optical axis, which allows for x-rays to be reflected to a common focus. Therefore the sagittal curvature of each plate is part of a circle centered on the optical axis. The meridional curvature is in a plane that encompasses the optical axis. In the case of SPO, where the source is at infinity, all the incident rays are parallel, and the meridional curvature will create a variation of the angle of incidence onto each plate as a function of the position along the optical axis. For SiLCs, the meridional curvature creates an angular bandpass or angular width for each crystal, similar to mosaicity. When the source is not at infinity, even a plate that does not have any meridional curvature is seen by the source as a range of angles: this is simply the angle subtended by the plate. Meridional curvature can be designed to match with this angle such that the rays diffracted at any point along the axis will be focused to a common point. This will also lead to a nearly monochromatic bandpass for each given plate. The sagittal and meridional curvatures lead to significantly improved focusing, which reduces the size of the point spread function (PSF) of the lens compared to unbent diffracting crystals. Indeed the size of the focal spot is no longer determined by the size of the individual single crystals but by the accuracy of the applied curvatures. This property leads to considerably higher signal-to-noise ratios than what is achievable with a conventional Laue lens design made of mosaic crystal tiles. Another distinct advantage is the reproducible quality of the materials which are compatible with large-scale production. The SiLCs are made of diced silicon wafers, which are commercially available with well-defined quality (i.e. purity, surface roughness, and total thickness variations). An illustration of a SiLC is shown in figure 1.
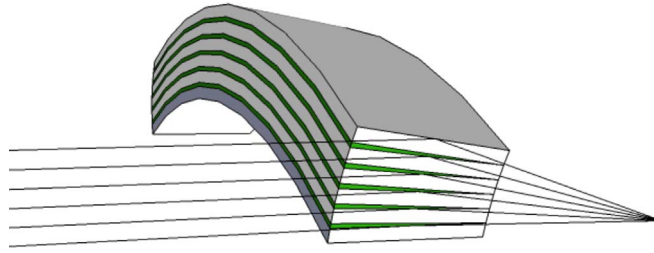
Figure 1. Illustration of a SiLC. The lines represent photons trajectories going from left to right. The green part represents the wedge (not to scale).
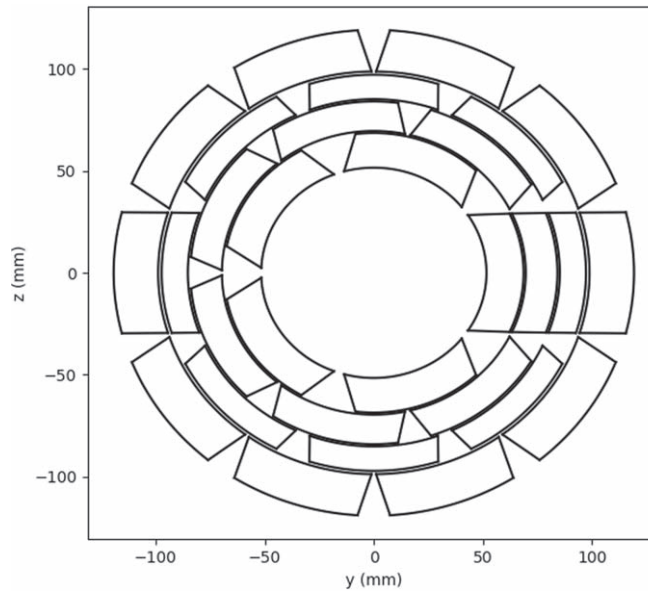

Figure 2. Example of a full lens consisting of multiple SiLCs in the *y–z* plane (plane perpendicular to the optical axis). The optical axis (*x*-axis) runs through the center of the lens.

Since the plates composing SiLCs are bent following arcs of circles, SiLCs can be used to populate concentric rings, whose center defines the optical axis. An example of this is shown in figure 2 where a full lens is displayed in the plane perpendicular to the optical axis. The optical axis runs through the center of the lens. Each SiLC has an inner and outer radius, which are related by the number of plates and their thickness. Multiple rings of SiLCs are present in this example.
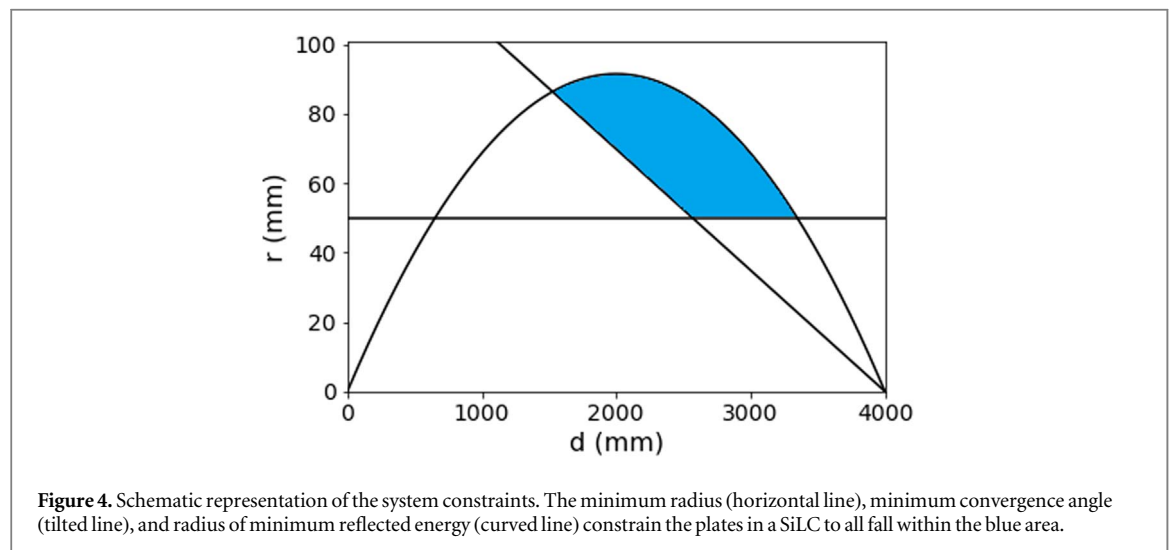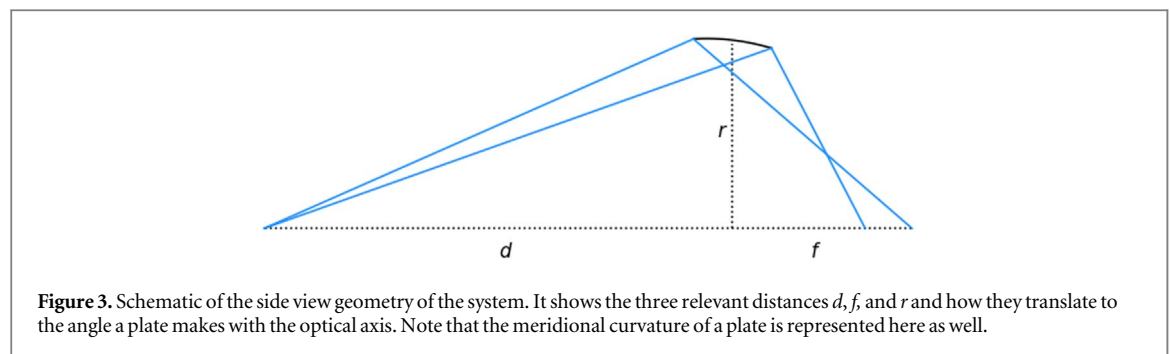
3. Lens design method

3.1. System parameters

It is useful to describe the geometry of the system in terms of the distance *d* between the source and lens, the distance *f* between the lens and focus, and the distance *r* of a plate to the optical axis. These distances are schematically shown in figure 3.

For fixed values of *d*, *f*, and *r*, the angle a plate makes with respect to the optical axis is fixed. Assuming the crystal planes are in the same plane as the plate surface, then d_{hkl} is known and the Bragg angle θ_{Bragg} can be determined by equation (2) and can be used to calculate the energy reflected at the center of the plate by using equation (1)

$$\theta_{Bragg} = \frac{\pi - \arctan\left(\frac{d}{r}\right) - \arctan\left(\frac{f}{r}\right)}{2}. \tag{2}$$

However, as plates are stacked on top of each other, the center of each plate will be at a different distance *r* from the optical axis and, therefore, also makes a different angle with the optical axis. Therefore each plate is given a wedge so that the plate on top of it also has the desired orientation. We thereby define two new system

Figure 3. Schematic of the side view geometry of the system. It shows the three relevant distances *d*, *f*, and *r* and how they translate to the angle a plate makes with the optical axis. Note that the meridional curvature of a plate is represented here as well.

Figure 4. Schematic representation of the system constraints. The minimum radius (horizontal line), minimum convergence angle (tilted line), and radius of minimum reflected energy (curved line) constrain the plates in a SiLC to all fall within the blue area.

parameters, the initial angle or the angle the bottom plate of a SiLC makes with the optical axis, and the wedge or the average wedge required to get all other plates in the right orientation.

The center of each plate in the SiLC will reflect a different energy, thus contributing to the energy bandpass of the lens. Additionally, each plate also has a bandpass determined by the Bragg angle corresponding to the front and the back of the plate (as seen from the source). This bandpass can be controlled by the length of the plate and its meridional curvature, which is the difference in orientation of the crystal planes between the front and the back of a plate. The method of determining the optimal plate length and meridional curvature is described in section 4.

3.2. System constraints

In the lens design presented in this paper, three different system constraints are being considered: the minimal radius, the minimal convergence angle, and the minimal energy. First, there is a physical limit to the elastic bending of silicon plates. If a certain curvature threshold is crossed, the plates will break. The bonding energy needs to be strong enough to counteract the spring force from the bent plates. For these reasons, a limit must be set on the radius *r* of the inner-most plate. Second, two factors of significant influence on the dose delivered to the skin are the convergence angle of the reflected x-rays and the energy of these x-rays. The convergence angle is defined as the angle between the diffracted rays and the optical axis. Finally, as the diffracted energy decreases with increasing *r*, the constraint of a minimal reflected energy E_{min} can be translated to a maximum allowable radius r_{max} of a plate by solving equation (2) for *r*.

The constraints on the minimum radius, maximum radius, and convergence angle are shown graphically in figure 4, for a fixed source to focus distance $d + f = 4$ m, as the horizontal line, curved line, and tilted line, respectively. All plates of the SiLC must then fall within the area highlighted in blue.

3.3. Dimensions and shape of the focus

It is essential to distinguish between the desired focal spot of the combination of all plates and the focal spot of a single plate. The initial angle and wedge of the plates will determine the position of the general focal spot, while the meridional curvature of a plate determines the position of its meridional focus. These two do not have to be in the same position in space. Moreover, as tumors are three-dimensional objects, it is crucial to consider the

Table 1. Focus-to-skin dose ratio for combinations of x-ray energy and convergence angle.

	100 keV	150 keV	200 keV	250 keV	300 keV
4.85°	12.6	16.1	17.4	20.2	21.0
3.24°	—	8.8	—	10.7	—
2.43°	5.1	5.9	6.9	7.7	8.2
1.95°	—	4.8	—	6.1	—
1.62°	3.3	3.8	4.6	5.1	5.5

focal spot in three dimensions. Therefore, it is chosen to take a value of the meridional curvature that focuses the x-rays before the desired focus. This choice creates the desired effect of extending the focus in the optical axis direction while simultaneously slightly increasing the meridional curvature, thus increasing the diffracted flux. From this geometry, we can define a value for the angular width as the difference between the angle on the left and right side of the plate (as displayed in figure 3). This approach leads to a relation between the meridional curvature and the plate length based on geometric considerations and not based on optimizing the reflectivity.

In this paper, it is chosen to find an optimized combination of angular width and plate length numerically for a given configuration. For application in radiation therapy, it is deemed more useful to deliver the maximum dose to the focal point rather than increasing the reflectivity and thereby also increasing the dose delivered to unwanted areas. Contrary to the sketch in figure 3, the rays do not stop at the focus, but rather keep going. The focus is thus three-dimensional, defined by the volume of highest dose deposition.

3.4. Energy versus convergence angle
In our system, there is a trade-off between energy diffracted and convergence angle. Indeed, convergence angle can be increased by either increasing the sagittal radius *r* of the plates, or by bringing the lens closer to the focus (decreasing *f*). In both cases, the deflection angle increases which results in lower diffracted energy. It is possible to compensate for these effects and increase the energy diffracted by using higher diffraction orders, but this comes at the expense of diffracted flux as the reflectivity rapidly decreases with higher order diffractions. Ultimately, the focus-to-skin dose ratio is the parameter that we want to maximize. So we investigate the effect of energy and convergence angle on this parameter to guide the lens design. We used Geant4 to simulate the dose distribution of a beam of mono-energetic x-rays converging to a focal point of 1 mm in diameter placed 10 cm deep within a water phantom, originating from an annulus with 8 and 9 cm inner and outer radius, respectively. The annulus was placed at various distances between 1 and 3 m from the focus, thereby varying the convergence angle. The energy of the x-rays was varied between 100 and 300 keV. From this simulation, we extracted the focus-to-skin dose ratio. The results are shown in table 1, here the lengths have been converted to the corresponding convergence angle.

The results show that increasing the energy from 100 to 300 keV hardly doubles the focus-to-skin dose ratio, while increasing the convergence angle from about 1.6° to about 4.9° almost quadruples this ratio. We conclude that a larger convergence angle should be favored over a large energy, given that it is not possible to have both due to the constraining relation between diffraction angle and energy.
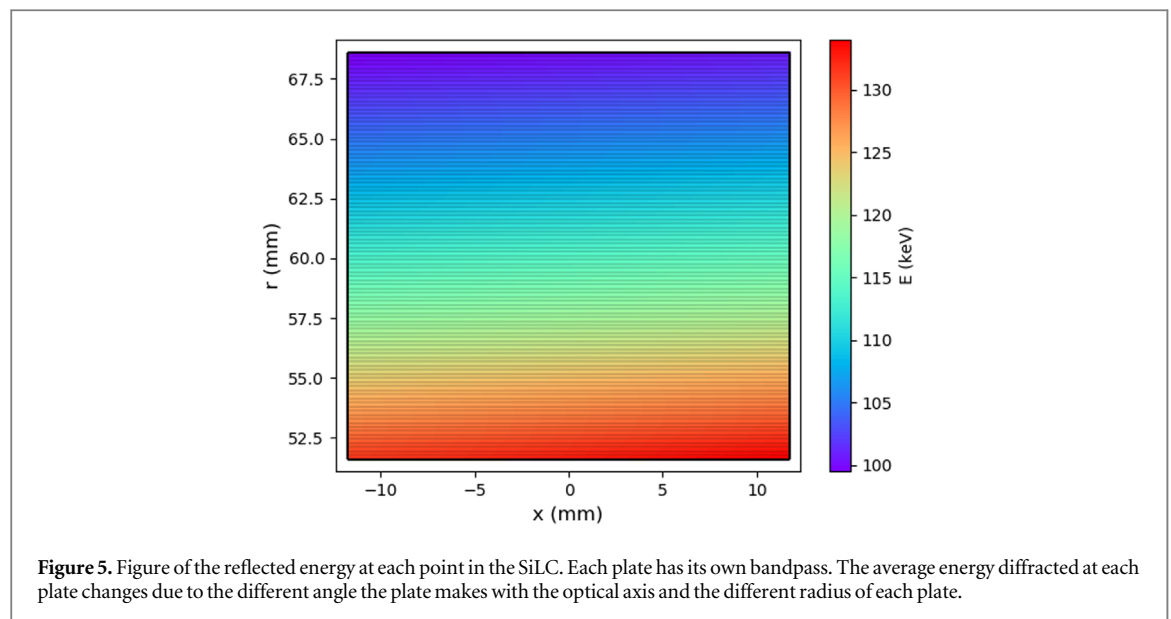
3.5. Diffraction orders
Lower diffraction orders result in higher reflectivity, but correspond to a smaller Bragg angle, resulting in a reduced convergence angle. Therefore, the choice of what diffraction order to use becomes a trade-off between reflectivity and convergence angle. As seen in the previous section, a larger convergence delivers higher focus-to-skin dose ratio and should be favored for radiotherapy. Therefore this problem can be dealt with using a simple rule of thumb: maximize the convergence angle using the lowest diffraction order possible.

3.6. SiLC reflectivity and spectrum
Assuming the x-ray source to be a point source, the energy diffracted at each point in a plate can be calculated. Figure 5 shows a meridional cut through a SiLC made of 100 plates of 170 μm thickness, and each point is colored based on the energy it diffracts.

An approximation of the reflected spectrum of this SiLC can be calculated, assuming most photons enter the SiLC through the side facing the source, rather than through the bottom side facing the optical axis. For this, it is assumed that the incoming spectrum is uniform with an intensity of 1 and that the contribution of each plate to the SiLC spectrum is uniform within its bandpass. Then, within the spectrum, each plate contributes only within the boundaries of its bandpass, and its contribution equals its reflectivity divided by the number of plates in the SiLC. Notice that for the situation where each plate would have an identical bandpass and reflectivity, the

Figure 5. Figure of the reflected energy at each point in the SiLC. Each plate has its own bandpass. The average energy diffracted at each plate changes due to the different angle the plate makes with the optical axis and the different radius of each plate.

spectrum would be uniform with a value of the plate's reflectivity and the plate bandpass width. Figure 5 shows that only a few plates will be able to diffract a given x-ray energy. Therefore, if an x-ray of this energy hits the SiLC anywhere, it only has a probability of being diffracted when it hits a plate in which it can diffract. We then define the effective reflectivity as the reflectivity divided by the number of plates in the SiLC. For example, if all plates diffracting a specific x-ray energy have an average reflectivity of 0.2, and 10 out of 100 plates can diffract this energy, then the effective reflectivity for this energy will be 0.02.

3.7. SiLC simulation code (SSC)

The properties of the design must be well understood to optimize the design for a SiLC lens. To this end, an in-house Monte Carlo ray trace code named SSC was developed to simulate the output of a given design when illuminated by a source characterized by its spectrum (e.g. tungsten anode x-ray tube, flat continuum, monochromatic) and spatial extent (e.g. point source, extended disc). The code was validated step by step, starting from the simplest geometry for which analytical calculation is trivial (single flat plate, point source with flat continuum spectrum). The results were then validated for each added level of complexity: plate with curvature, stack of plates, stack of plates with curvature, and finally stack of plates separated by a thin wedge. In a lens design, the PSF is affected by many parameters, including the dimensions of the individual plates, the number of plates in a stack, Miller index of diffracting planes, and the radii of meridional curvature. The SSC uses ray-tracing and diffraction physics to facilitate the study and optimization of different lens designs. The code is used to test the spectral and spatial properties of the PSF produced by a lens design when illuminated by a given source. The code generates photons with randomized origins (for an extended source), directions, and energies based on distributions defined by a particular source such as an x-ray generator for simulating testing conditions. Ray-tracing is used to calculate which plates a given photon interacts with and the entrance and exit points of the photon for each of those plates. Since the plates are bent in two directions (sagittal and meridional), the normal of the diffracting plane changes along a photon's path through a plate. This change complicates the calculations estimating the probability of different interactions the photon may have (transmission, diffraction, or absorption). To calculate the probability of these interactions, the model for distorted crystals described by Malgrange (2002) is used. If diffraction occurs, a new photon is generated, and its path through the lens is measured to test for multiple reflections. When photons are first generated, they are given an intensity of 1. As reflections occur, the intensity is appropriately decreased. Put another way, the code calculates the possible positions where an incoming photon can undergo diffraction and the subsequent direction of travel. The intensity values assigned to a photon reflect the probability of it exiting the lens in that particular state (coordinate of diffraction and direction of travel). After all photons (transmitted and reflected) have exited the lens, an absorption correction is applied corresponding to each photon's path length through the lens and the photons' energy.
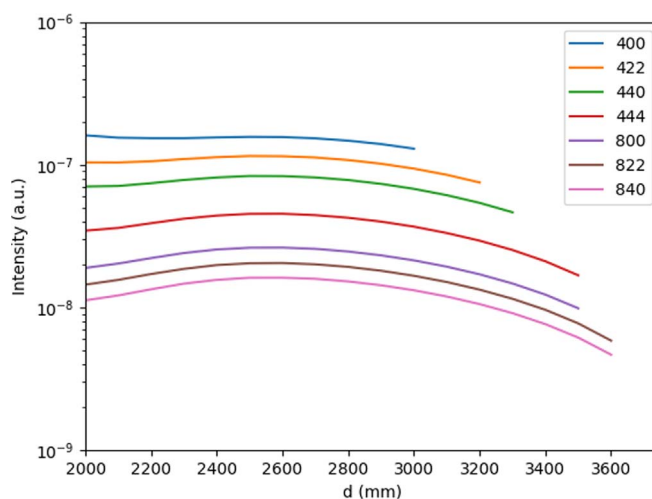
Figure 6. Reflected intensity curves of different diffraction orders for a total system length of 4 m and a minimal reflected energy of 100 keV.

4. Optimized lens design

This section describes the parameters and performance of the optimized Laue lens system. It makes choices on system parameters described in section 3.

4.1. Decisions on the system parameters

Before a design can be optimized, some parameters and limits of the system need to be fixed. These are the total system length, the focal point depth, the minimum radius, the minimal x-ray energy, and the source size. A total system length of 4 m has been chosen. This length of the system is larger than most existing systems but should be practical at least for prototype designs, and allows the use of the relatively efficient 400 diffraction order. To get a small enough focal point, a focal point depth of 5 mm has been chosen. A minimum sagittal radius of 50 mm is considered, which is considered realistically achievable. A minimal x-ray energy of 100 keV is chosen, as going lower would result in rapidly increasing photo-electric absorption in silicon. The data shown in section 3.4 shows that 100 keV x-rays could result in a better focus/skin dose ratio than 300 keV, as the lower energy x-rays come in at larger angles. Furthermore, the decision has been made to look for a middle ground between reflected intensity and convergence angle. Finally, the optimization process was performed for a source size of 2 mm, which is deemed realistic for high-intensity x-ray tubes.

4.2. Optimization process

The highest achievable reflected intensity for different diffraction orders as a function of d is shown in figure 6. For each value of d, the intensity is shown for the optimal combination of plate length and meridional curvature. A small increase in the total reflected intensity is seen when moving the lens away from the symmetric point ($d = 2000$ mm) and closer to the focal point. There, the increase in meridional curvature compensates for the lower x-ray flux hitting the lens with higher reflected intensity due to an increase in the bandpass of the plates. It is clear that the most critical factor in determining the total reflected intensity is the used diffraction order. It is chosen to only use the first four diffraction orders satisfying our criteria presented in figure 4 (400, 422, 440, and 444). The next diffraction order, 800, would increase the total diffracted flux only by a few percent given that its effective reflectivity is an order of magnitude lower than that of 400. It is thereby decided that it is not worth pursuing this option.

Lastly, a decision needs to be made on the position of the lens and the thickness of the SiLC. Planarity and surface roughness usually degrade as silicon wafers thickness becomes smaller. Besides, we want to minimize the number of plates per SiLC. Therefore we chose the maximum thickness allowing the bending and bonding of plates. The plate thickness is fixed to 170 μm based on previous studies (Girou *et al* 2017), and the number of plates determines the thickness of the SiLC. It has been shown in section 3.4 that the convergence angle is of great importance for the focus/skin dose ratio. The convergence angle can be maximized by placing the lens as close to the focus as possible. Figure 6 shows that using the 400 diffraction order, the closest the lens can be placed to the source is as $d = 3000$ mm.
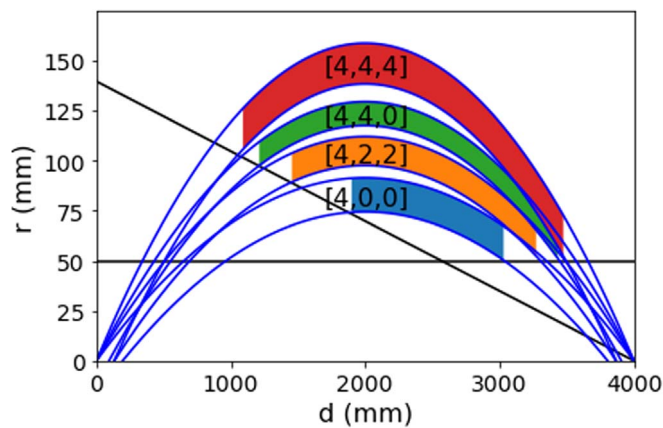
Figure 7. Range of *r* at which the SiLCs of the lens design are located as a function of *d*. The colored areas denote the allowed positions of each SiLC within the system constraints.

Table 2. The parameters of the final lens design used in Monte Carlo method and Geant4 simulations. All rings are made of silicon plates 170 μm thick and 60 mm wide.

	Ring 1	Ring 2	Ring 3	Ring 4
hkl	400	422	440	444
Inner radius (mm)	51.6	69.6	85.3	98.8
Number of plates	100	85	70	120
Plate length (mm)	23.5	25.0	24.5	25.0
Initial angle (°)	0.98	1.33	1.62	1.88
Wedge (arcsec)	11.63	11.59	11.55	11.49
Angular width (arcmin)	2.75	3.76	4.41	5.70

Figure 7 shows for each value of *d* what range of *r* would be occupied by a SiLC of the four chosen diffraction orders. It shows intuitively that a significant gain in convergence angle can be attained by placing the lens at $d = 3000$ mm, therefore this position is adopted in the lens design. It must be ensured that the SiLCs do not overlap radially at this position, which results in the choice of 100, 85, 70, and 120 plates for the 400, 422, 440, and 444 diffraction order, respectively. These choices result in the lens design of which all parameters are listed in table 2.

4.3. Performance

The performance of the lens system has been assessed using first SSC simulations and then Geant4 for dose calculations. These simulations were performed for an x-ray tube source operating at 200 kV with a source diameter of 2 mm calculated with SpekCalc software (Poludniowski *et al* 2009, Poludniowski and Evans 2007, Poludniowski 2007). The resulting reflected spectrum is shown in figure 8. It shows that the lens diffracts x-rays between 100 and 135 keV. The peak intensity is around 100 keV, as the design imposes that all SiLCs reflect here. Around 115 and 122 keV, two large steps in the reflected intensity are observed. These large steps are caused by some SiLCs having a smaller bandpass than others, so at these energies some SiLCs in the lens stop contributing the diffracted spectrum. Also, the peak of the bremsstrahlung in the source spectrum is around 85 keV. The diffracted spectrum of figure 8 lies close to this peak. An x-ray tube operating at a slightly higher voltage could be used as a small optimization.

To account for attenuation and estimate the dose deposition rate of this system, we performed Geant4 simulations with Monte Carlo data. A phase space file produced by the lens code is imported in Geant4 with positions, directions, energy, and intensity coefficient of each photon diffracted by the lens. SSC simulations have been performed using an x-ray source with a diameter of 2 mm. The x-ray profile 10 cm before the focal point is shown in figure 9. The x-rays coming from each SiLC can still be separated very well.

Figure 10 shows the x-ray profile at the focal point. It shows how the x-ray flux intensity is approximately 100 times higher than 10 cm before the focal point.

Figure 11 displays a cross-section of the dose deposition in a water phantom, assuming the lens is used with a 3 kW x-ray tube operated at 200 kV (15 mA). The focus is 10 cm deep into the water phantom. It clearly shows a
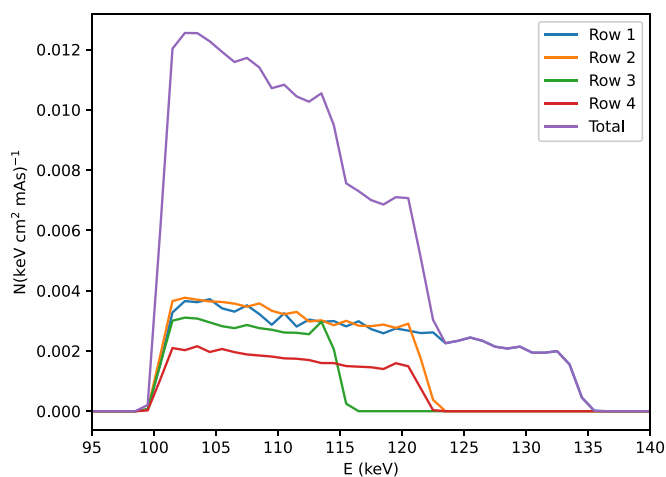
Figure 8. The spectrum reflected by the lens design using a 200 kVp x-ray tube source. This spectrum is generated by Monte Carlo method simulations.
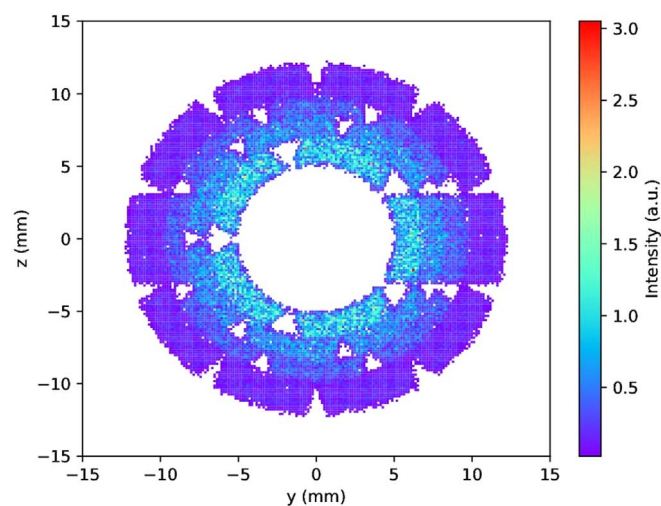

Figure 9. X-ray profile 10 cm before the focal point (i.e. at the 'skin') for a simulated source diameter of 2 mm.
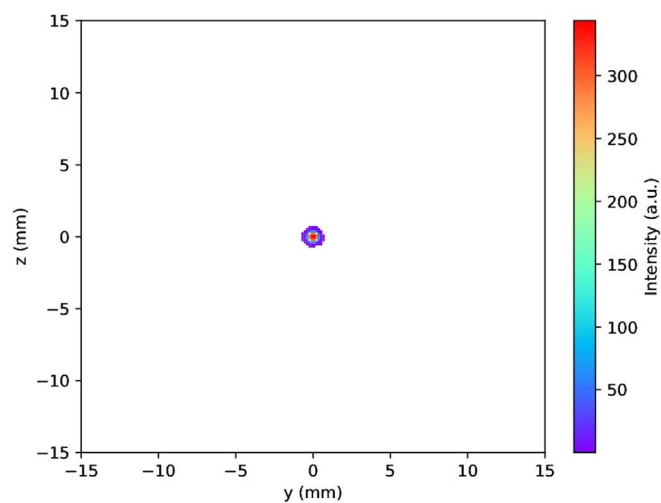

Figure 10. X-ray profile at the focal point for a simulated source diameter of 2 mm.
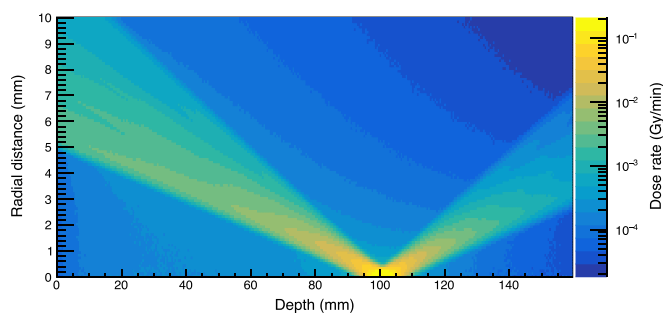
Figure 11. Cross section of the dose rate deposition in a water phantom. The optimized lens design was used together with a 2 mm source diameter. This data was generated using Geant4 fed with the output of the python ray-trace code.

Figure 12. Maximum dose rate delivered as a function of depth into a water phantom. The optimized lens design was used together with a 2 mm source diameter. This data was generated using Geant4 fed with the output of the python ray-trace code.
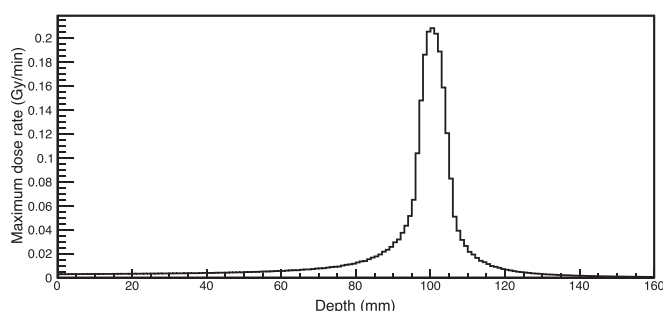
much higher dose rate at the focal point (depth = 100 mm) than at the skin (depth = 0 mm). Note that the dose here refers to the absorbed dose that is the energy deposited per unit mass. The focal spot is cylinder shaped, with a diameter of 0.7 mm and a length of 10 mm.

Figure 12 shows the maximum dose rate delivered as a function of depth into the water phantom. The dose rate at the focal point is 72 times higher than the dose rate at the skin. Using a 3 kW x-ray tube, a dose rate of approximately 0.2 Gy min^{-1} is achieved at the focus.

The dose rate we obtain here is ∼50 lower than in the study of a Laue lens for radiation therapy published by Paternò *et al* (2016). This study is complemented by the paper from Camattari (2017), which gives details on the treatment of diffraction in crystals that is used to produce this estimated dose rate. The fact that their study is based on a somewhat different Laue lens can not explain the dose rate difference. We concluded after much effort that their higher dose rate is likely due to an erroneous treatment of diffraction in crystals when the source is placed at finite distance, which was confirmed by the authors [private communication].

5. Conclusions and future work

We designed and studied a Laue lens that can focus radiation in a cylindrical volume of 0.7 mm diameter and 10 mm long when coupled to an x-ray tube with a source size of 2 mm diameter. A dose rate of 0.2 Gy min^{-1} can be achieved at the focus placed 10 cm within a water phantom considering a 15 mA anode current set to 200 kV. This dose rate is 72 times more than the dose rate at the entrance of the volume. Thus this system can produce a very high focus-to-skin ratio with a small, sharp focus and relatively low dose rate. It should be noted that we studied here an ideal case and that errors in positioning and alignment will affect the performance of an actual system. A sensitivity study will be performed at a later stage.

Several hurdles need to be overcome before this could be translated into a meaningful clinical device. The first is the dose rate. Since a typical radiation therapy treatment requires a dose of approximately 2–10 Gy to the tumor in a single fraction, at the dose rates simulated here the treatment time is 10–50 min. While this is not unreasonable the irradiated volume is a small 0.7 × 10 mm cylinder whereas typical target volumes might require a 10 × 10 × 10 cm^3 volume. At the current dose rate, the time would be prohibitively long if the spot were scanned over this volume, and the skin sparing effect would be reduced. However, the technology is attractive since such a device could be a cost-effective option for treating tumors, particularly where sharp

gradients in dose distribution are needed. Given the dose rate and geometry constraints, this might be better suited to smaller target regions <10 cm deep in tissue.

Other applications, such as x- and gamma-ray astronomy (Lund 1992, 2005), could also benefit from SiLC. Hard x-ray astronomy in the energy range up to 200 keV is currently limited by the low signal-to-noise ratio above ~78 keV, at which point the effective area afforded by the current generation multi-layer mirrors decreases quickly (Harrison *et al* 2013), while the background does not. Laue lenses use Bragg diffraction to concentrate gamma-rays and therefore decouple the collecting area and the detector volume leading to an increase in sensitivity. Many areas of astrophysics would, however, benefit significantly from new observational constraints in the 78–200 keV range. Polarization measurements combined with timing capabilities could distinguish between competing models for pulsar magnetospheres; the emission mechanisms in the jets of microquasars and AGN could be distinguished (synchrotron or inverse Compton); Also, the regions of strong gravitational fields near black holes where high-energy emission is produced could be studied.

Acknowledgments

Disclosures

The authors declare no conflicts of interest.

ORCID iDs

David Girou ● https://orcid.org/0000-0003-1062-9390

References

Abbas H, Mahato D N, Satti J and MacDonald C A 2014 Measurements and simulations of focused beam for orthovoltage therapy *Med. Phys.* **41** 041702

Abrosimov N V *et al* 2005 Growth and properties of Ge1-xSix mosaic single crystals for γ-ray lens application *J. Cryst. Growth* **275** e495–500

Ackermann M, Barrière N M, Collon M J, Günther R, Vacanti G, Beijersbergen M W and Haneveld J 2013 Bending and bonding Si single crystals for high performance Laue lenses *Optics for EUV, X-Ray, and Gamma-Ray Astronomy VI* vol 8861 ed S L O'Dell and G Pareschi (SPIE) p 88610G

Agostinelli S *et al* 2003 GEANT4—a simulation toolkit *Nucl. Instrum. Methods Phys. Res* A **506** 250–303

Allen C, Her S and Jaffray D A 2017 Radiotherapy for cancer: present and future *Adv. Drug Delivery Rev.* **109** 1–2

Allison J *et al* 2006 Geant4 developments and applications *IEEE Trans. Nucl. Sci.* **53** 270–8

Allison J *et al* 2016 Recent developments in GEANT4 *Nucl. Instrum. Methods Phys. Res.* A **835** 186–225

Atun R *et al* 2015 Expanding global access to radiotherapy *Lancet Oncol.* **16** 1153–86

Barrière N, von Ballmoos P, Bastie P, Courtois P, Abrosimov N V, Andersen K, Halloin H, Skinner G and Smither R K 2006 Second generation crystals for Laue lens applications *Space Telescopes and Instrumentation II: Ultraviolet to Gamma Ray* vol 6266 ed M J L Turner and G Hasinger (SPIE) p 62662D

Barrière N M, Tomsick J A, Boggs S E, Lowell A, Wade C, Baugh M, von Ballmoos P, Abrosimov N V and Hanlon L 2014 Developing a method for soft gamma-ray Laue lens assembly and calibration *Nucl. Instrum. Methods Phys. Res.* A **741** 47–56

Bavdaz M *et al* 2019 Optics developments for ATHENA *Optics for EUV, X-Ray, and Gamma-Ray Astronomy IX* vol 11119 ed S L O'Dell and G Pareschi (International Society for Optics and Photonics, (SPIE)) pp 71–82

Barrière N, von Ballmoos P, Natalucci L, Roudil G, Bastie P, Courtois P, Jentschel M, Abrosimov N V and Rousselle J 2017 Laue lens: the challenge of focusing gamma rays *Proc. SPIE* **10566** 1056603

Beijersbergen M, Kraft S, Günther R, Mieremet A L, Collon M, Bavdaz M, Lumb D H and Peacock A J 2004 Silicon pore optics: novel lightweight high-resolution x-ray optics developed for XEUS *UV and Gamma-Ray Space Telescope Systems* vol 5488 ed G Hasinger and M J L Turner (International Society for Optics and Photonics, SPIE) pp 868–74

Bellucci V, Camattari R, Guidi V, Neri I and Barrière N 2011 Self-standing bent silicon crystals for very high efficiency Laue lens *Exp. Astron.* **31** 45–58

Berbeco R I, Korideck H, Ngwa W, Kumar R, Patel J, Sridhar S, Johnson S, Price B D, Kimmelman A and Makrigiorgos G M 2012 DNA damage enhancement from gold nanoparticles for clinical MV photon beams *Radiation Research* **178** 604–8

Breitkreutz D Y, Weil M D, Zavgorodni S and Bazalova-Carter M 2017 Monte Carlo simulations of a kilovoltage external beam radiotherapy system on phantoms and breast patients *Med. Phys.* **44** 6548–59

Camattari R 2017 Laue lens for radiotherapy applications through a focused hard x-ray beam: a feasibility study on requirements and tolerances *Phys. Med. Biol.* **62** 7249

Chithrani D B, Jelveh S, Jalali F, Van Prooijen M, Allen C, Bristow R G, Hill R P and Jaffray D A 2010 Gold nanoparticles as radiation sensitizers in cancer therapy *Radiat. Res.* **173** 719–28

Collon M J *et al* 2019 Status of the silicon pore optics technology *Optics for EUV, X-Ray, and Gamma-Ray Astronomy IX* vol 11119 ed S L O'Dell and G Pareschi (International Society for Optics and Photonics, SPIE) pp 150–7

Demaria S, Bhardwaj N, McBride W H and Formenti S C 2005 Combining radiotherapy and immunotherapy: a revived partnership *Int. J. Radiat. Oncol. Biol. Phys.* **63** 655–66

Desouky O, Ding N and Zhou G 2015 Targeted and non-targeted effects of ionizing radiation *J. Radiat. Res. Appl. Sci.* **8** 247–54

Ferrari C, Buffagni E, Bonnini E and Korytar D 2013 High diffraction efficiency in crystals curved by surface damage *J. Appl. Crystallogr.* **46** 1576–81

Frontera F and von Ballmoos P 2010 Laue Gamma-Ray lenses for space astrophysics: status and prospects *X-Ray Optics and Instrumentation* **2010** 215375

Girou D, Wade C, Barrière N, Collon M, Günther R, Hanlon L, Tomsick J, Uliyanov A, Vacanti G and Zoglauer A 2017 Development of a second generation SiLC-based Laue lens *Optics for EUV, X-Ray, and Gamma-Ray Astronomy VIII* vol 10399 ed S L O'Dell and G Pareschi (International Society for Optics and Photonics, SPIE) pp 419–23

Guidorzi C *et al* 2021 A deep study of the high-energy transient sky *Exp. Astron.* (https://doi.org/10.1007/s10686-021-09725-9)

Halloin H and Bastie P 2005 Laue diffraction lenses for astrophysics: theoretical concepts *Exp. Astron.* **20** 151–70

Halloin H *et al* 2003 Society of photo-optical instrumentation engineers (spie) conference series *Society of Photo-Optical Instrumentation Engineers (SPIE) Conf. Series* vol 4851 ed J E Truemper and H D Tananbaum pp 895–904

Harrison F A *et al* 2013 The nuclear spectroscopic telescope array (NuSTAR) mission *Astrophys. J.* **770** 103

Keitel S, Malgrange C, Niemöller T and Schneider J R 1999 Diffraction of 100 to 200 keV x-rays from an Si1-xGex gradient crystal: Comparison with results from dynamical theory *Acta Crystallogr.* A **55** 855–63

Khan F 2003 The physics of radiation therapy *LWW Doody's All Reviewed Collection* (Lippincott Williams & Wilkins)

Leung M K, Chow J C, Chithrani B D, Lee M J, Oms B and Jaffray D A 2011 Irradiation of gold nanoparticles by x-rays: Monte Carlo simulation of dose enhancements and the spatial properties of the secondary electrons production *Med. Phys.* **38** 624–31

Lindquist T R and Webber W R 1968 A focusing x-ray telescope for use in the study of extraterrestrial x-ray sources in the energy range 20–140 keV *Can. J. Phys. Suppl.* **46** 1103

Lund N 1992 A study of focusing telescopes for soft gamma rays *Exp. Astron.* **2** 259–73

Lund N 2005 An 'eSA-affordable' Laue-lens *Exp. Astron.* **20** 211–7

Malgrange C 2002 X-ray propagation in distorted crystals: from dynamical to kinematical theory *Cryst. Res. Technol.* **37** 654–62

Maszara W P, Goetz G, Caviglia A and McKitterick J B 1988 Bonding of silicon wafers for silicon-on-insulator *J. Appl. Phys.* **64** 4943–50

Paternò G, Marziani M, Camattari R, Bellucci V, Mazzolari A, Gambaccini M and Guidi V 2016 Laue lens to focus an x-ray beam for radiation therapy *J. Appl. Crystallogr.* **49** 468–78

Poludniowski G, Landry G, Deblois F, Evans P M and Verhaegen F 2009 SpekCalc: a program to calculate photon spectra from tungsten anode x-ray tubes *Phys. Med. Biol.* **54** N433

Poludniowski G G 2007 Calculation of x-ray spectra emerging from an x-ray tube: II. X-ray production and filtration in x-ray targets *Med. Phys.* **34** 2175–86

Poludniowski G G and Evans P M 2007 Calculation of x-ray spectra emerging from an x-ray tube: I. Electron penetration characteristics in x-ray targets *Med. Phys.* **34** 2164–74

Shimbo M, Furukawa K, Fukuda K and Tanzawa K 1986 Silicon-to-silicon direct bonding method *J. Appl. Phys.* **60** 2987–9

Smither R, Saleem K A, Beno M, Kurtz C, Khounsary A and Abrosimov N 2005 Diffraction efficiency and diffraction bandwidth of thermal-gradient and composition-gradient crystals *Rev. Sci. Instrum.* **76** 1–19

Wade C, Barrière N, Tomsick J, Hanlon L, Boggs S, Lowell A, von Ballmoos P and Massahi S 2018 Construction, characterization, and environmental testing of a Laue lens prototype using Fe and Al crystals *Nucl. Instrum. Methods Phys. Res.* A **895** 135–43